Scilight

Progress in Composite Materials
https://www.sciltp.com/journals/pcm

Article

Impact of Rare Earth Particulates Addition on the Wear Rate of Magnesium Composites with Improved Mechanical and Microstructural Properties for Orthopedic Applications

Divyanshu Aggarwal [1,*], Siddharth Sharma [2] and Manoj Gupta [3,*]

[1] Department of Mechanical Engineering, Thapar Institute of Engineering and Technology, Patiala 147004, Punjab, India
[2] Department of Biotechnology Engineering, Thapar Institute of Engineering and Technology, Patiala 147004, Punjab, India
[3] Department of Mechanical Engineering, National University of Singapore, 9 Engineering Drive 1, Singapore 117576, Singapore
* Correspondence: divyanshuaggarwal95@gmail.com (D.A.); mpegm@nus.edu.sg (M.G.); Tel.: +91-8591093067 (D.A.); +65-166358 (M.G.)

How To Cite: Aggarwal, D.; Sharma, S.; Gupta, M. Impact of Rare Earth Particulates Addition on the Wear Rate of Magnesium Composites with Improved Mechanical and Microstructural Properties for Orthopedic Applications. *Progress in Composite Materials* **2025**, *1*(1), 2. https://doi.org/10.53941/pcm.2025.100002

Received: 18 July 2024
Revised: 22 August 2024
Accepted: 30 August 2024
Published: 9 September 2024

Abstract: This study aims to evaluate the wear rate of Mg-Hydroxyapatite-based composites reinforced with rare earth oxide (Neodymium oxide) under in-vitro physiological conditions along with mechanical and microstructural evaluations. To analyze the wear rates of the composites, an innovative technique has been designed to perform experiments on the fabricated samples. The counter disc used for interaction was stainless steel disc coated with the same material as the samples. The analysis was performed under different loading conditions with different sliding velocities considering the different compositions of rare-earth oxide (1%, 1.5%, and 2%). The samples were fabricated via powder metallurgy route with compaction pressure of 250 MPa followed by sintering at 400 °C for 2 Hrs. Moreover, the mechanical analysis was done by calculating the samples' microhardness and ultimate tensile strength. In contrast, the materials were characterized and synthesized employing FTIR, FESEM, XRD, and EDS techniques. The lowest wear rate was observed when the samples were subjected to higher load and lower velocities. Also, it was found that during progressive wear testing, the wear rate is maximum in the initial stage, but with the increase in sliding distance, the wear rate tends to reduce and then become steady. In addition, it was found that Mg-HA-1.5Nd_2O_3 showed the highest wear resistance. Moreover, the microhardness of the sample with a rare-earth concentration of 1.5% was higher as compared to other samples. Similar results were obtained for ultimate tensile testing of the composites. FESEM images showed refined microstructure of the samples, with EDS results showing the homogenous distribution of HA and REO particles. XRD analysis showed the development of secondary β-phases that interlocks grain boundaries. Hence, the designed experimental setup provides extensive wear rate results with related conditions created when the implant is placed inside the physiological environment.

Keywords: Mg-Hydroxyapatite composites; neodymium oxide; wear analysis; mechanical properties; microstructure

1. Introduction

In recent decades, there has been a rapid advancement in biomaterial composites for orthopedic applications. Metals and their alloys have traditionally been extensively used across industries for manufacturing components of varying complexity, due to their superior strength, wear resistance, ease of extraction, and machinability compared to ceramics and polymers. Despite these advantages, metals face significant challenges related to friction and wear, particularly under physiological conditions, raising concerns about their long-term degradation [1,2]. To address these issues, global research efforts have focused on enhancing metals, ceramics, and polymers by reinforcing them with more robust and stiffer elements, thereby improving their properties for both existing and future technologies. These enhanced materials, known as composites, consist of two or more distinct physical or chemical phases, leading to characteristics that surpass those of the individual components [3–5]. The development of composites has made it possible to significantly improve the properties of even low-strength alloys. Additionally, numerous studies have shown that incorporating various reinforcements into the matrix of composites can notably enhance their frictional properties [6–9].

Compared with traditional biomedical alloys/composites, Magnesium (Mg)-based bio-composites and bio-alloys have been employed in various biomedical applications such as bone fixation, cardiovascular stents, hip joints, screws/pins, and dental implants. The RDI (recommended daily intake) of magnesium is nearly 200–400 g, which makes it a suitable material for the implant [10–12]. The main problem with the implant material is their toxicity after degradation in the body and excretion of its eroded particles from the body. The use of magnesium can resolve these issues. Although, the biggest challenge in using magnesium is its rapid degradation. This can be reduced by adding various reinforcing elements in the magnesium. Although pure magnesium demonstrates generally suitable corrosion properties as an implant material for resorbable applications, it frequently possesses insufficient mechanical properties. By means of alloying with appropriate alloying elements, it is possible to eliminate the mechanical deficiencies of pure magnesium. In addition to this, magnesium possesses desirable mechanical properties (density: 1.74 g/cm^3; elastic modulus 45 GPa, and compressive yield strength 65–100 MPa) closer to those of natural bone, which minimizes the disturbance of bone growth as well as problem of stress shielding [13,14]. The inferior surface properties such as low wear resistance and higher corrosion rates of Mg based materials have restricted its applications in the orthopedic industry. The physiological conditions consist of a harsh acidic environment that can degrade the materials followed by interfacial wear due to bone-implant or implant-implant interactions. Moreover, the wear debris produced due to such interactions can cause early implant failure before resorption of the bone. Various research has been performed to eradicate these issues upto some extent. Mankari et al. [15] conducted a study on the wear resistance of Mg/glass micro-balloon (GMB) syntactic foams by a disintegrated melt deposition method. The wear analysis was performed at a velocity of 3 m/s at a constant load of 30 N for a sliding distance of 600 m with abrasion and oxidation as the primary wear mechanisms. The study concluded the successful incorporation of hollow GMB particles with the improved wear resistance of approx. 2.5 times that of pure Mg. Another research performed by Mu et al. [16] utilized sputter coating of TiZrNb films over the Ti_6Al_4V substrates for enhancing the wear and corrosion resistance of the matrix. The study revealed that with the increase in coating thickness, the development of β-phases increased, forming a strong intermetallic structure to resist corrosion and wear rate. Moreover, the improvement in wear and corrosion rates were approx. 34.3% and 65.7%, respectively, at 120 W power deposition. Chirico et al. [17] developed a low-cost powder metallurgy β-titanium alloy for biomedical applications with improved wear resistance. The study introduced two strategies, i.e., nitriding the surface and reinforcing with TiN particles, to revamp the corrosion resistance of the alloy. Dry sliding wear testing (at different loading conditions) analyzed that wear resistance was improved by the modification techniques and the alloys' hardness.

In this regard, the current study focuses on developing a novel technique to analyze the wear mechanism of Mg-Hydroxyapatite-based biomedical composites. Also, very few studies have been performed to investigate the wear performance of biomedical composites under the physiological environment with the conventional wear analysis pin-on-disc tribometer technique. To improve the composite wear resistance, rare-earth oxide, i.e., Neodymium oxide, has been reinforced with the matrix. Rare earth oxides (REO) have been used extensively to improve the metal alloys and composites' surface integrity and microstructural characteristics. Moreover, the hard intermetallic phases developed by the addition of rare earth oxide particulates control grain growth's anisotropy and resistance to dislocation movement [18–20]. Therefore, the proposed methodology introduces the utilization of REO for biomedical implant applications to improve the wear resistance of Mg-based bio-composites.

2. Materials and Methods

2.1. Setup

The experimental setup for the wear rate analysis is shown in Figure 1a, whereas for better picturization, a schematic diagram has been made and depicted in Figure 2. It consists of interaction between the fabricated sample and stainless-steel disc with a diameter of 160 mm (Hardness: 220 HV) and spray coated with the same material as the sample as shown in Figure 1b. The specimen is placed above the disc with the help of a pin-holder with adjustable clamps, followed by rotation of the disc via an electric AC motor. Under physiological conditions, the sample and the rotary plate were immersed inside the Phosphate buffer saline (PBS) solution (pH = 7.4 ± 2). During the operating conditions, the sample is kept in a stationary state, clamped with the pin holders, whereas the counter disc is left in a rotating condition for a specific time to calculate the progressive wear rates of the samples. The PBS was covered with a glass lid to resist any contamination in the solution, with a small spacing provided for the sample to enter the container containing the disc and PBS solution. The whole casing was placed in a specified growth room with a temperature 37 °C to provide optimum conditions for the experiment. The sliding speed and load variations were controlled via a controller connected to the test setup. The clamping unit adjusts the sliding distance from the center of the friction disc.

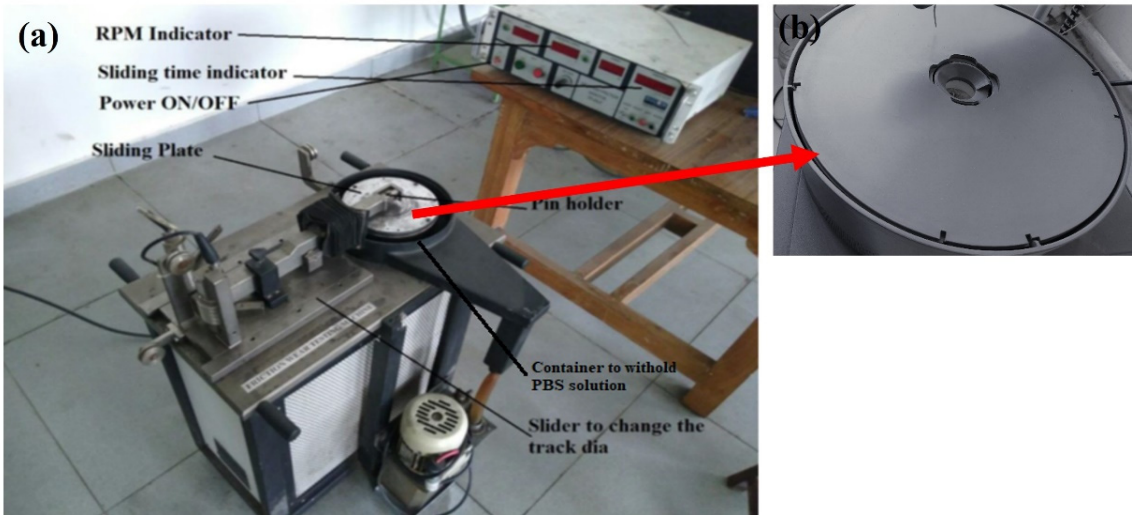

Figure 1. (**a**) Experimental setup for wear analysis (**b**) Mg-HA-Nd_2O_3 coated Friction disc.

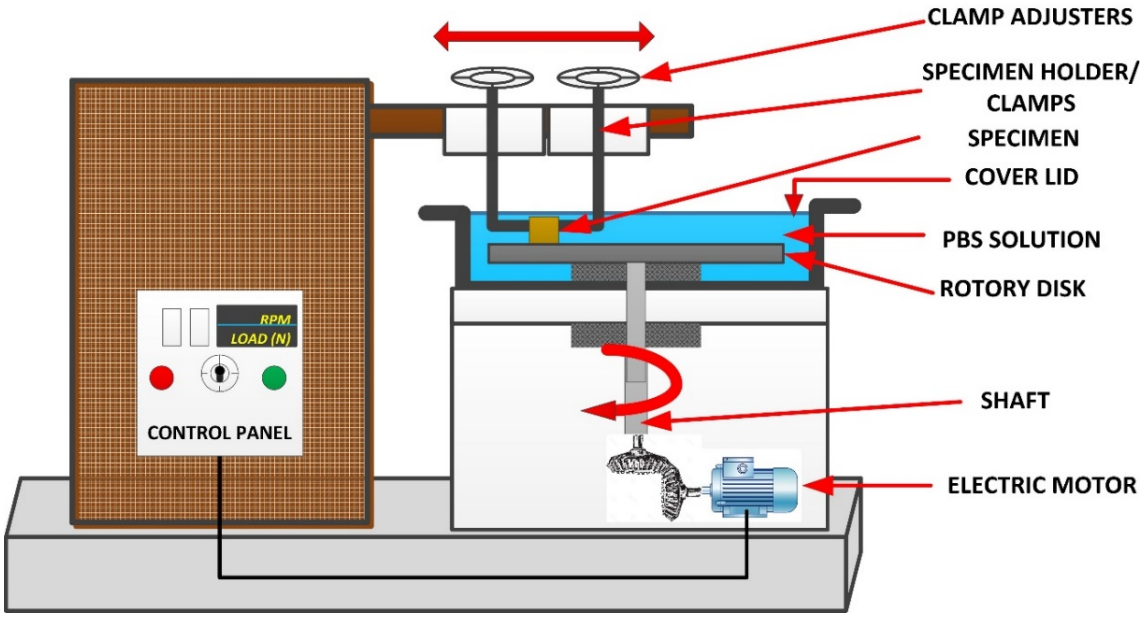

Figure 2. Schematic representation of wear analysis setup.

This technique provides in-vitro wear analysis of the samples under physiological conditions, which was not possible to date. The paramount wearing of the implants is due to interaction with the wear debris and the similar

surface [21,22]. Therefore, the counter surface was developed by coating the steel disc with the same material as that of the test sample to provide similar conditions for the implant when placed inside the body. Although this technique does not offer a precise performance analysis of the biomedical implant, further modifications can increase the technology's viability.

2.2. Material Preparation

Magnesium powder (≤0.1 mm) was purchased from Fine laboratory chemicals, Mumbai, India and were mixed with 10 wt% Hydroxyapatite (HA) ($Ca_{10}(PO_4)(OH)_2$) particles (10 µm, Sigma Aldrich, USA). Along with HA, three different concentrations of Nd_2O_3 (1, 1.5, and 2 wt%) were added as reinforcement and the mixture was allowed to mix via ball mill at 120 RPM for 2 h. The rare-earth oxide was purchased from Subra Scientific Company, Chennai, India, with a particle size of 10 µm. The milled samples were put into a Stainless-steel die (Diameter 10 mm) and uniaxially compressed at 250 MPa using a Hydraulic pellet pressing machine (PCI analytics Mumbai). For sintering purposes, the samples were placed in a Tubular furnace under inert gas atmosphere (Argon) and were allowed to sinter at a temperature of 450 °C for two hours. The samples obtained after heat treatment were of the size 10 mm × 7 mm with different concentrations, as shown in Table 1. The prepared samples were then allowed to cool down under vacuum for 12 h and were taken out afterward for further experimentations

Table 1. Composition of different elements present in the samples.

Sample	Mg, %wt	$Ca_{10}(PO_4)(OH)_2$, %wt	Nd_2O_3, %wt	Sample Code
Mg-HA-1 Nd_2O_3	Balance	10	1	A
Mg-HA-1 Nd_2O_3	Balance	10	1.5	B
Mg-HA-1 Nd_2O_3	Balance	10	2	C
Mg-HA	Balance	10	n.a	D

2.3. Characterization

The procured materials (in powder form) were characterized using Fourier Transform Infrared (FTIR) spectroscopy technique (Shimadzu- QATR 10, Kyoto, Japan) with a spectrum range between 500–4000 cm^{-1}. Moreover, the prepared composite, after sintering, was grounded to powder to compare the effects of heat treatment on the absorbance of the composite powders. The samples were cleaned using 400, 800, and 1200 grit emery paper to develop a clean surface for microstructure characterization. Afterward, the samples were etched with 5% HNO_3 solution followed by washing with DI water. The samples were then kept under a desiccator attached to a vacuum pump to dry out the samples. Various techniques were used to analyze the microstructural data of the samples. For phase identification, the X-ray diffraction (XRD) technique (Malvern Panalytical, Malvern, UK) was used with a scanning range (2Θ) from 20–110° having K-alpha2/K-alpha1 ratio as 0.5 and step size 0.01313. The different patterns of the samples were analyzed through 'X-PERT High score' software. To study the surface topography of the samples, Field emission scanning electron microscopy (FESEM) assisted with energy dispersive spectroscopy (EDS) techniques (ZEISS, Sigma 500, Taufkirchen, Germany) were utilized.

2.4. Sliding Friction Test

The cylindrical pin shapes (10 mm × 7 mm) developed for the wear analysis were allowed to slide over a friction disc with the same surface as the sample under different parametrical conditions. The different loading conditions, sliding distance, and velocity were adjusted with the help of the control panel, and the values of the set parameters are shown in Table 2. Before starting the experiment, all the samples were grounded by emery paper of different grades (400, 800, 1000). Afterward, the samples and the friction disc were taken out after every cycle, cleaned with 5% Chromic acid, and washed with DI water to remove the debris from the surface. The wear rates were assessed by calculating the weight loss of the samples as a function of sliding distance, as shown in Equation (1). Microstructure analysis was performed to analyze the effect of different loading conditions on the wear rate of the samples and the development of several cracks and surface defects.

$$\text{Wear rate (mg/m)} = \frac{\text{Weight Loss } (\Delta w)}{\text{Sliding distance (m)}} \quad (1)$$

Table 2. Details of sliding wear parameters.

Parameters	Description
Test specimens	1. Mg-HAP-1Nd_2O_3 2. Mg-HAP-1.5Nd_2O_3 3. Mg-HAP-2Nd_2O_3 4. Mg-HAP
Counter disc	Stainless steel coated with Mg-HAP- Nd_2O_3 Diameter = 160 mm
Sliding Distance (m)	500, 1000, 1500, 2000
Sliding Velocity (m/s)	0.5, 1, 1.5
Normal Loads (N)	10, 20, 30
Lubrication Conditions	PBS solution (pH = 7.4 ± 2)
Temperature (°C)	37 °C

2.5. Mechanical and Wettability Testing

The microhardness of the samples was assessed via Vicker's hardness tester (Metatech Industries, Pune, India) with a 20 gm load and 15 s dwell time. Moreover, the ultimate tensile strength of the samples was calculated using ZwickRoell tensile tester (Capacity: 10 kN). The specimens of size 45 mm × 10 mm × 10 mm were prepared for the experiment. Each experiment was performed in triplicates, and finally, the average value was taken. Contact angles were measured via contact angle measurement technique to determine the surface hydrophobicity of the fabricated samples (Easy Drop, Hamburg, Germany). A sessile drop analyzer was used to assess the contact angle calculations. The drop images were captured in the direction perpendicular to the surface, and a total of twenty repetitions were done to generate results.

3. Results and Discussions

3.1. FTIR Spectroscopy

Figure 3 represents the FTIR spectra of the materials before fabrication and after fabrication. The spectra were obtained to analyze the different bonding modes and chemical characteristics of the materials utilized in the current study. Moreover, the sample produced after sintering was also analyzed to investigate the change in the bonding structure of the compounds after heat treatment. The FTIR spectrum of both the REO and HAP powders were recorded and compared with the Mg-HAP-1.5NdO composite powder. The composite spectra show similar peaks at 3608.87 cm^{-1} as that of NdO. This depicts the presence of NdO functional groups after sintering at 400 °C. The presence of alkynes, i.e., -C≡C-H and C-H bend, and weak N-H bonds were revealed at 649.05 cm^{-1} and 1478.86 cm^{-1}, respectively, in NdO microparticles. In addition, the peak at 3608.87 cm^{-1} shows a strong O-H stretch and H-bonded alcohol and phenols. This strong band participated actively in the Mg-HAP-NdO composite after heat treatment. These peaks were associated with the spectrums highlighted in understudies performed by Lembang et al. [23] and Ahmadi et al. [24]. However, a broader weak spectrum was observed for the composite at 1030.96 cm^{-1}, like HAP. The presence of PO_4^{3-} and HPO_4^{2-} groups was depicted in the HAP powder at 1030.96 cm^{-1} and 558.401 cm^{-1} peaks, respectively. These results were in correlation to the data reported in the literature [25,26]. Moreover, a broad -OH stretched spectrum region was observed for all Mg and HAP powder materials between 3550 cm^{-1} and 3700 cm^{-1}. The results showed that after sintering, several bonds present in the individual powder materials were still present, which shows the homogeneous bonding of the particles in the composites.

3.2. Microstructure

The XRD and EDS results are shown in Figure 4a,b. As shown in XRD images, the heat treatment of the samples produced various secondary intermetallic phases such as $Mg_{12}Nd$, $Ca_8MgNd(PO_4)_7$, and $CaCO_3$. Being highest in concentration, Mg showed the most extended peak at 37°, 34°, and 64°. The development of various intermetallic phases was confirmed through X'PERT data collection software by identifying different 'd' values. The study revealed that when the rare earth oxide composition was above 1.5%, the peaks were broad as compared to the peaks shown by the samples with a 1.5% composition addition. The broader peaks showed low refinement of grains whereas, as the peak becomes narrow and sharp, the refinement of grains occurs [27]. Intermetallic phases have the property of providing interlocking between the grain boundaries, which results in resistance to grain growth as well as barricading dislocations. The divorced eutectic phase, i.e., $Mg_{12}Nd$ was observed in all the samples due to inhomogeneous solution developed at some proportions of the composites. However, when the rare earth oxide with a %age composition of 1.5% was added to the matrix, its peaks tended to decrease, showing the reinforcement's homogenous distribution. In addition, $CaCO_3$ formation provided solid structural integrity to the

matrix, resulting in a hard brittle structure for the composites. Also, it can be observed from EDS images the reinforcements were homogeneously distributed across the grain boundaries of the α-Mg matrix, providing a pinning effect to the dislocation.

Moreover, the microcracks developed over the surface were adequately filled by the Ca and Nd particulates. The samples' elemental mapping provided clear insight into the reinforcement distribution in the composites. Hence, it can be concluded that the addition of rare earth oxide imparts strong intermetallic structure to the composite by developing several β-eutectic phases that provide a combination of pinning dislocation and cease the grain growth.

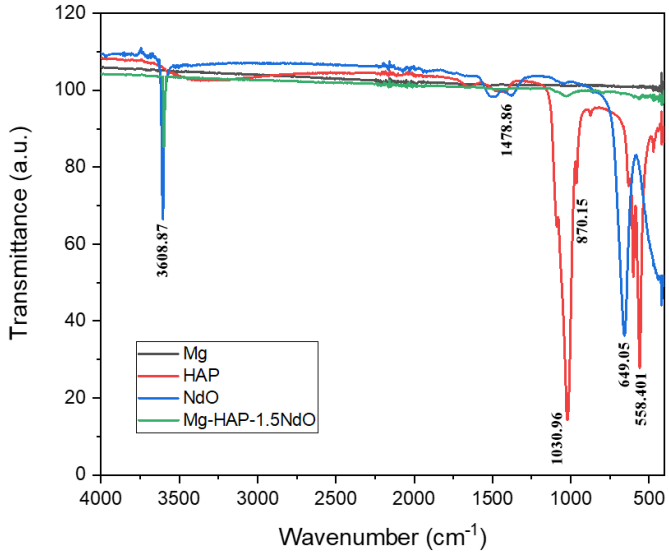

Figure 3. FTIR spectra of the powder materials.

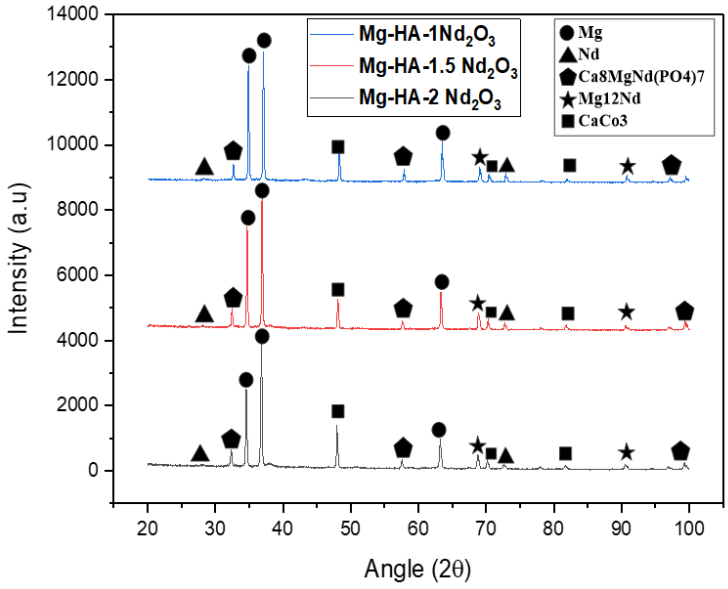

(a)

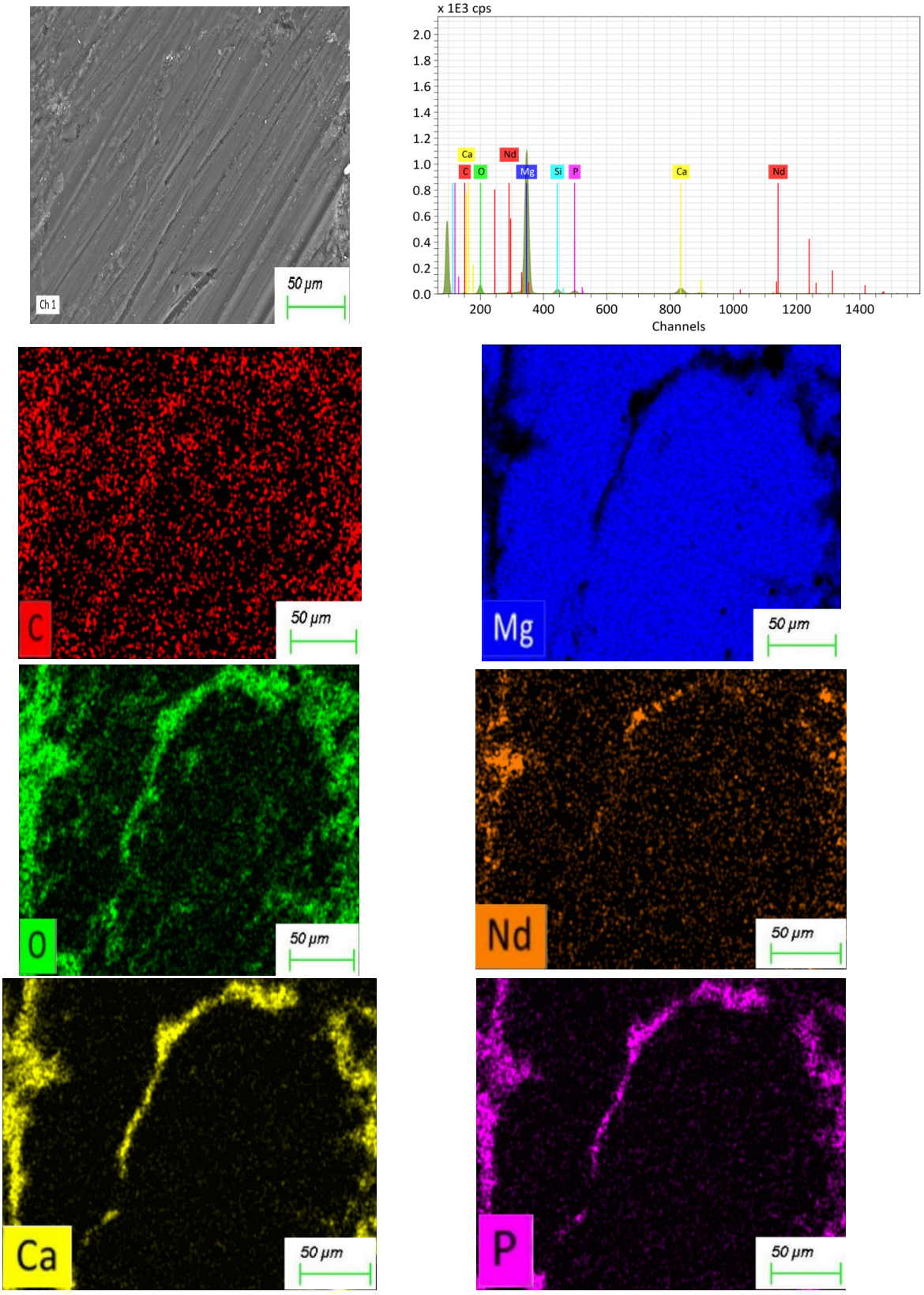

(**b**)

Figure 4. (**a**) XRD pattern of Mg-HA-xNd_2O_3 (x- 1, 1.5, 2%) (**b**) EDS spectra and elemental mapping of Mg-HA-2Nd_2O_3.

3.3. Mechanical Properties

3.4. Sliding Wear Test

For wear analysis, the samples were tested under different loading conditions keeping in mind the physiological conditions during which the implant undergoes several load variations due to the patient's movement. The wear testing under PBS solution develops a clear insight into the composites' wear. As seen from Equations (2)–(5), when Mg reacts with an aqueous solution, it creates a hydroxide layer over the surface and liberation of hydrogen gas. This results in increased corrosion of the samples as the evolution of H_2 gas generates gas pockets around the tissue, increasing the local pH level and reducing the healing of bone [40,41]. Moreover, the development of the hydroxide layer further reduces the corrosion by barricading the fluid from interacting with the substrate surface. However, this can also give rise to enhanced corrosion rates; when this hydroxide layer breaks, it will cause a sudden increase in corrosion due to thin oxide layer formation according to the Pilling-Bedworth ratio (<1). Similar effects were observed during the wearing of the samples when subjected to the implant-implant interaction mechanism under PBS solution, as discussed in the below sections

$$Mg + 2H_2O \rightarrow Mg(OH)_2 + H_2 \quad (2)$$

$$Mg \rightarrow Mg^{2+} + 2e^- \quad (3)$$

$$2H_2O + 2e^- \rightarrow H_2 + 2OH^- \quad (4)$$

$$Mg^{2+} + 2OH^- \rightarrow Mg(OH)_2 \quad (5)$$

The graph shown in Figure 7 denotes the effect of variation in Normal load (N) on the coefficient of friction (COF) of the developed specimens at different sliding velocities. It can be observed that the highest COF value corresponds to the lowest value of the load and at lowest sliding distance. As the load increased, there was a sudden decline in the value of COF with an increase in sliding distance. Furthermore, the composite consisting of 1.5% REO showed the lowest value of COF whereas, with 1% REO addition, the values were higher. However, with the addition of 2% REO, the value of COF was higher than 1.5% REO but lower than 1% REO composites. This can be attributed to the formation of a hard oxide layer over the surface of composites which reduced the surface wear out due to friction between the friction plate and the sample. Moreover, as discussed earlier, the presence of a higher amount of REO particulates in the composites (>1.5%) generated heavy agglomeration over the surface of the composites. In addition, the lower amount of REO (<1.5%) produces a non-homogeneous distribution of particles in the matrix pool. Hence, these factors led to increased values of COF concerning normal load. As the sliding velocity increases, the COF decreases. This can be due to the decline in friction between the disc and the specimen due to an increase in the contact area of the surfaces with increasing velocity. Therefore, the order of COF was found to be 1%>2%>1.5% under different loading conditions and sliding velocities.

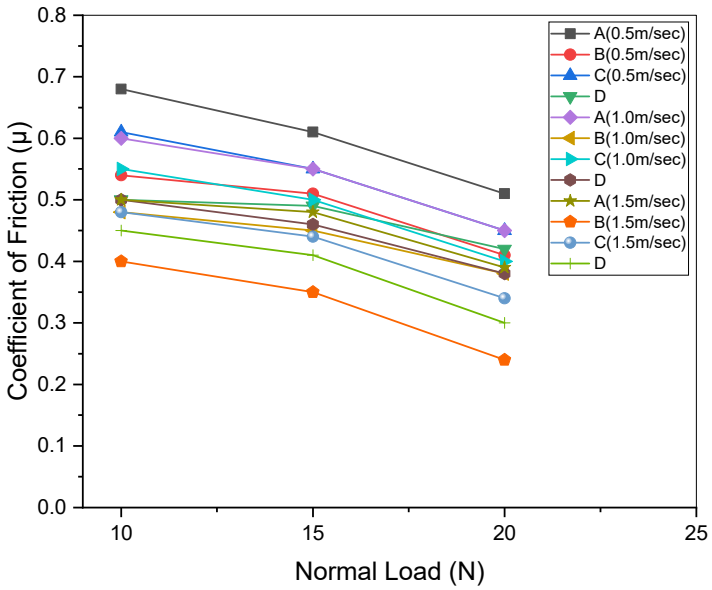

Figure 7. Plot showing Coefficient of Friction vs. Normal load variations (b).

3.4.1. Wear Mechanism at 10 N Load

FESEM images of the wear samples under a physiological environment, subjected to PBS, are shown in Figure 8a. Also, a graphical representation of wear rate vs. sliding distance is depicted in Figure 8b. It can be assessed that during low loading conditions, several defects such as pits and plastic deformation of the surface are developed due to the samples' wear. When the %age composition of rare earth oxide was below 1.5%, oxide formation was high at the initial stage, forming local sites for corrosion. This results in the premature wearing of the sample. As the sliding distance increases, the wear rate becomes constant. This can be due to the gap created between the interface of the friction disc and sample due to initial wear. Moreover, when the %age Nd_2O_3 was 2%, surface pitting started forming due to brittle fracture caused due to excessive hard reinforcement addition. However, when 1.5% of rare earth oxide was added, no such surface defects occurred under low loading conditions. Although plastic deformation of the surface was observed in the specimen, the surface remains intact under harsh physiological conditions.

Furthermore, it can be assessed from the results that at low sliding velocity, i.e., 0.5 m/s, the wear rate was low, but as the velocity increased, the wear rate increased. Abrasion was observed to be the primary wear mechanism for the wear of the samples. In addition, as the wear progresses, the intergranular cracks and microgrooves start to expand by continuous friction with the surface along with Cl^- ions present in the PBS solution.

It can be observed from XRD micrographs that when the REO addition was below 1.5%, hard intermetallic phase formation was low; this results in easy worn out of the particles from the composite pool; hence, increasing the wear volume as depicted in FESEM images. But, when the REO concentration was 1.5%, it became difficult to detach the HA and Nd_2O_3 from the α-Mg matrix phase due to secondary β-phase $Mg_{12}Nd$. Further increase in REO concentration generates heavy agglomeration and coarsening of the composite grains, resulting in weak structure and more prone to wear and tear. The EDS elemental mapping of the sample is shown in Figure 9. It provided promising data, giving a clear insight into the distribution of elements in the composites. The green color showed the oxide layer formed over the surface that was also observed under FESEM images of the samples. Moreover, all the samples showed better wear resistance as compared to Mg-HAP samples under lower loading conditions at low sliding velocities.

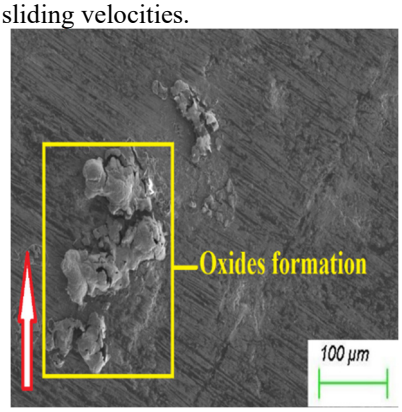

(**a1**)

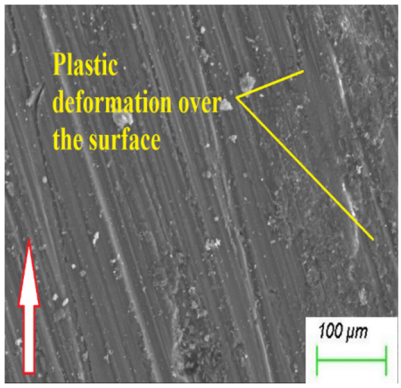

(**a2**)

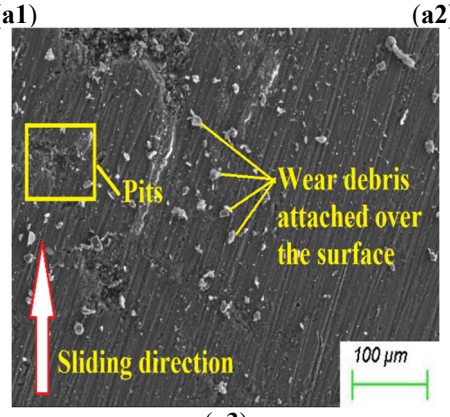

(**a3**)

(**a**)

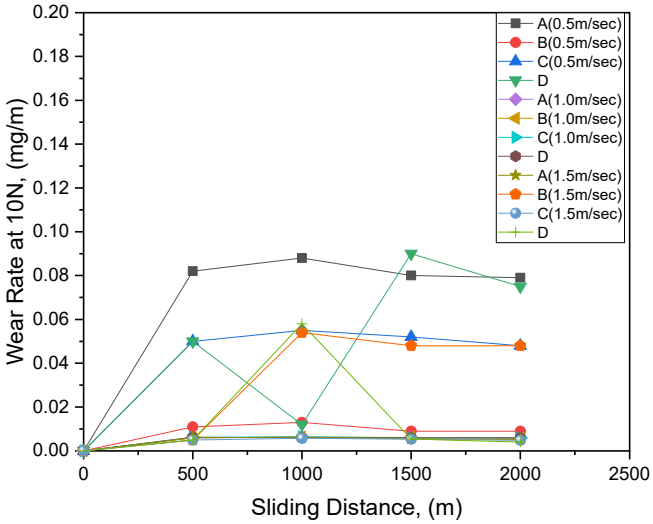

(**b**)

Figure 8. (**a**) Wear surface at 10N load (**a1**) Mg-HAP-1Nd_2O_3 (**a2**) Mg-HAP-1.5Nd_2O_3 (**a3**) Mg-HAP-2Nd_2O_3 (**b**) Progressive wear rate plot for composite samples at 10N load.

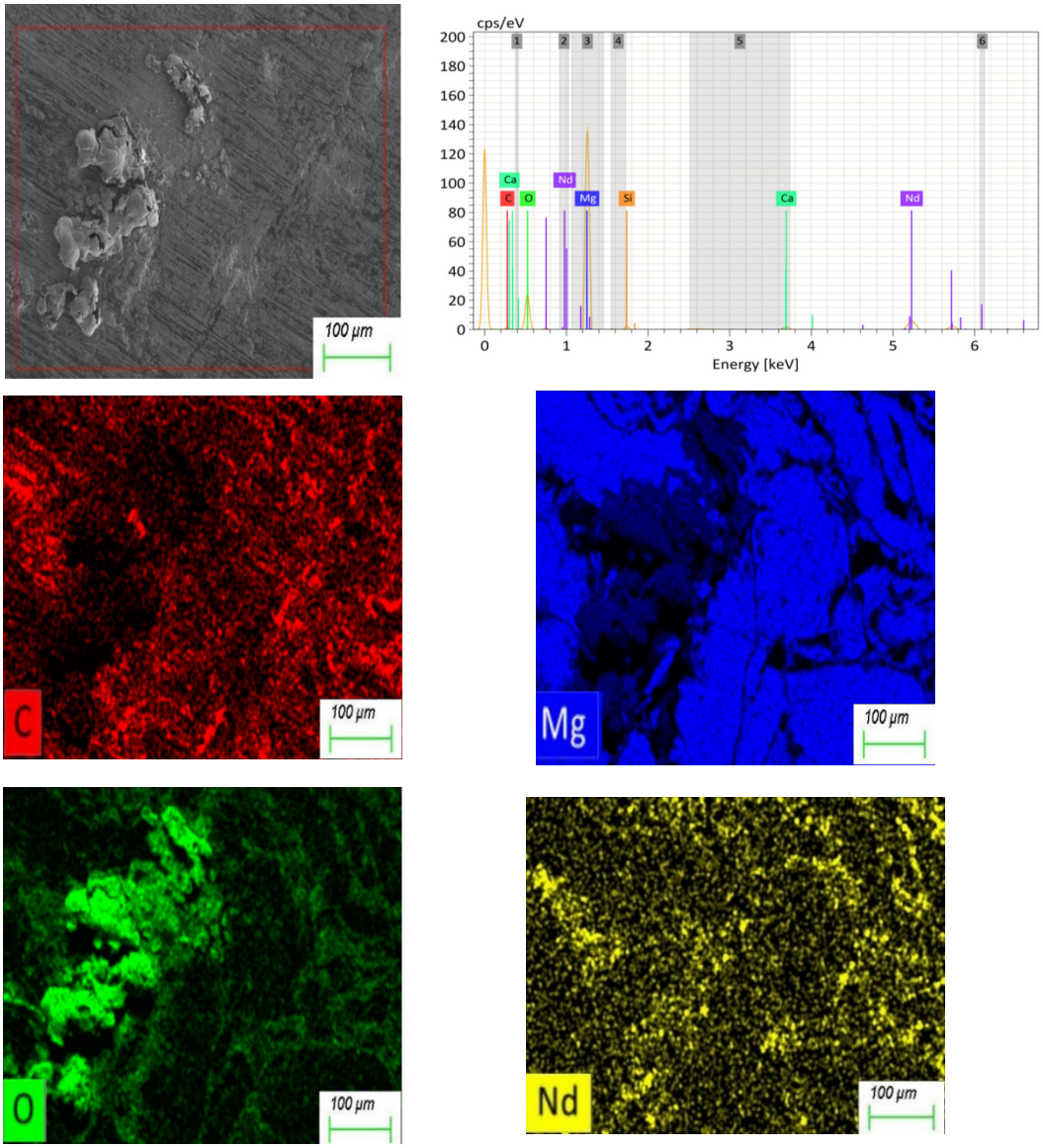

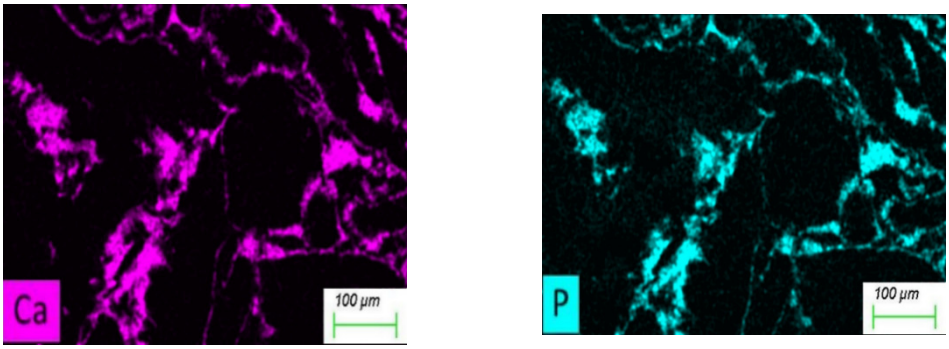

Figure 9. EDS spectra and elemental mapping of Mg-HA-1Nd_2O_3 composite samples at 10 N load.

3.4.2. Wear Mechanism at 15 N Load

The FESEM images of the wear samples under 15 N load are shown in Figure 10a. It can be observed that ploughing, delamination, and heavy pitting are the significant features that were noticed under higher loading conditions. Moreover, a higher amount of wear debris was deposited over the surface, which shows more broken surfaces when reinforcement was below 1.5%. At 2% addition, heavy pitting occurred due to surface cracking and reaction with physiological fluid. However, surface cracks were the major defects observed, with the sample having 1.5% Nd_2O_3 addition. The defects were more intense as compared to the samples subjected to 10 N load. A similar wear rate trend was observed under 15 N load as with 10 N loading, as shown in Figure 10b. The samples underwent a rapid wear rate till the sliding distance of 1000 m was reached, and after that, it became constant. As can be seen from micrograph images, the surface cracks may have increased the volume of wear rate, causing abrasion wear of the samples.

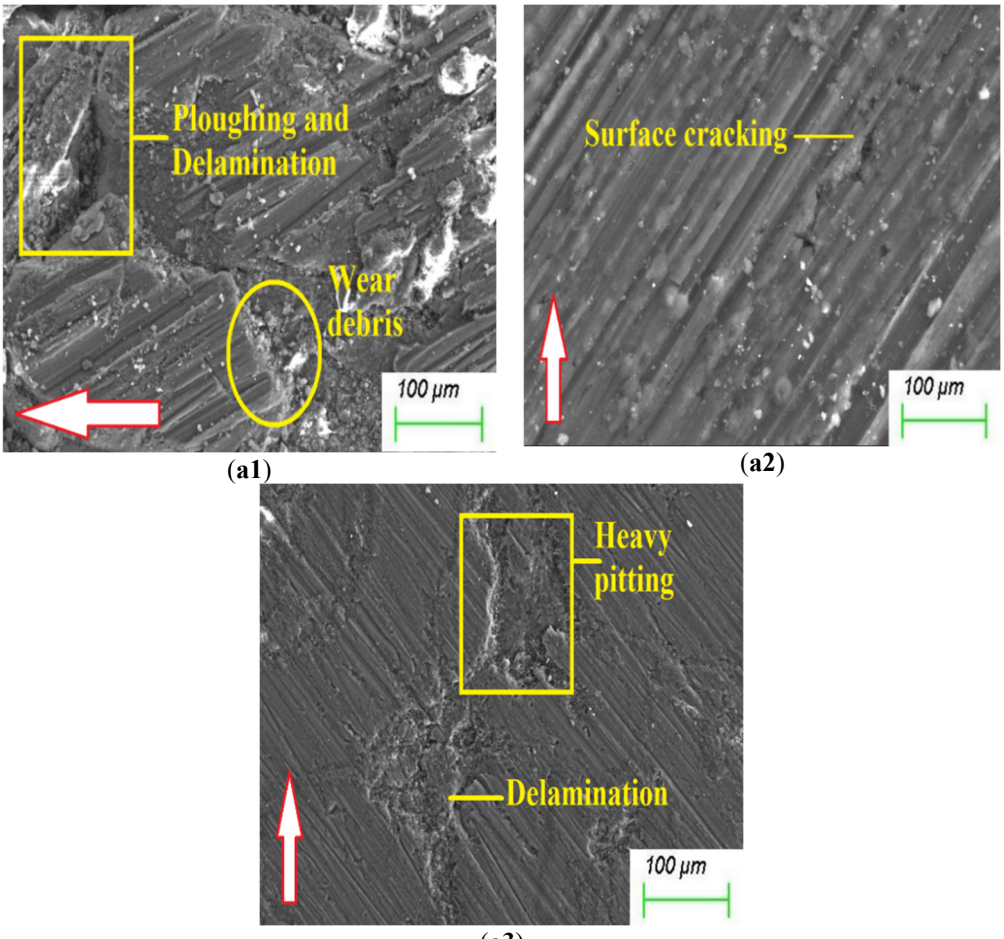

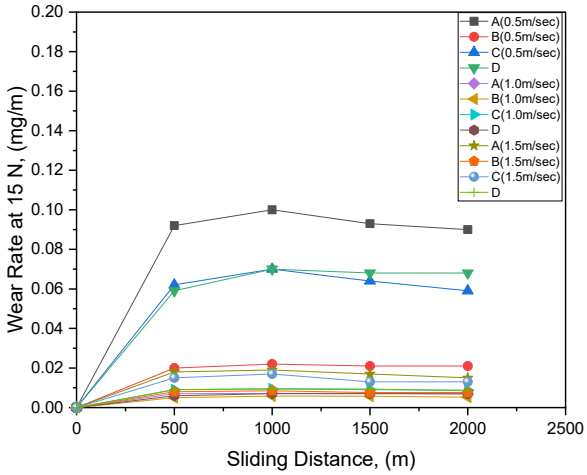

(**b**)

Figure 10. (**a**) Wear surface at sliding velocity 15 N load (**a1**) Mg-HAP-1Nd_2O_3 (**a2**) Mg-HAP-1.5Nd_2O_3(**a3**) Mg-HAP-2Nd_2O_3 (**b**) Progressive wear rate plot for composite samples at 15 N load.

Moreover, the generation of surface grooves and cracking can be due to the ploughing action of the wear surface caused due to hard intermetallic interaction as well as corrosion due to reagents present in PBS solution. The presence of secondary β-phases has a significant effect on the wear rate of the samples. As analyzed from the XRD diffraction technique, the presence of these phases is higher in the case of Mg-HA-1.5Nd2O3 composites, which results in a reduction of wear rate compared to other composites.

3.4.3. Wear Mechanism at 20 N Load

Figure 11a demonstrates the FESEM images of composites subjected to 30 N load under PBS solution. The images give a clear insight into the composites' precarious surface destruction under heavy loading conditions. The increase in load develops massive frictional contact between the interacting surfaces followed by the rapid wearing of the samples providing a pathway for PBS solvents to enter the composites, resulting in tearing the samples from inside at a rapid rate. Moreover, various pores were formed in the composites, reflecting the leaching of the particles due to reaction with PBS solution. Several other types of wear mechanisms can be observed from micrograph images. It can be marked that the needle-shaped elongated trench was formed due to the disintegration of divorced eutectic phases and secondary β-phases during the experiment. Also, it can be observed from Figure 11b that the initial wear rates showed escalated curves in all the samples like other loading conditions. As the distance between friction disc and composites increased, their interaction reduced, causing a constant wear rate of the samples. In addition, the PBS particulates were garnered on the surface of the composites, which gives a clear insight of surface degradation due to reaction with Cl^- ions present in the solution. The addition of 1.5% rare earth oxide to the composites showed a lower wear rate than other samples due to hard intermetallic bonding with the α-Mg matrix and Ca particulates.

3.5. Contact Angle Measurements

Figure 12a showed the wettability analysis of the composites via contact angle measurement technique using the sessile drop method. The sample incorporated with 1.5% rare earth oxides showed better results as compared to other samples. The average contact angle for Mg-HA-1.5Nd_2O_3 samples was seen to be 84° as demonstrated in Figure 12b, whereas the average contact angle for Mg-HA-2Nd_2O_3 and Mg-HA-1Nd_2O_3 was 77.7° and 65.1°, respectively. These values were more significant than that of the matrix (Mg-HA). It can be assessed from FESEM micrographs that the samples having a higher level of hydrophilicity tend to adhere more wear debris and PBS particulates, as shown in Figure 8a, 10a and 11a. The wear debris is responsible for the generation of several micro grooves and surface cracks which further enhanced the wear rate of the composites [42]. Moreover, the high wettability of the composites allowed the PBS particles to adhere to the surface, causing more degradation of the samples. In contrast, composites with 1.5% rare earth oxide content showed better surface wettability with lower hydrophilicity than other samples as it does not allow the wear debris and buffer solution to settle over the surface in high concentration. This results in lower wear rates and surface degradation.

Moreover, the shielding effect of the outermost electrons over the unfilled electrons in 4f orbitals of rare earth oxide materials reduces the bonding capacity with the water molecules [43,44]. This develops hydrophobicity over

the surface and hence reduces wettability. In addition, surface energy plays a vital role in enhancing hydrophobicity. Although a reduction in surface polarity leads to a decrease in surface energy with an increase in %age addition of rare earth oxide [45,46], which improves the hydrophobicity, higher concentration (above 1.5%) reversed the conditions. Hence, this results in better surface wettability of the rare-earth oxide composite samples and provides a good surface for successive wear inhibition.

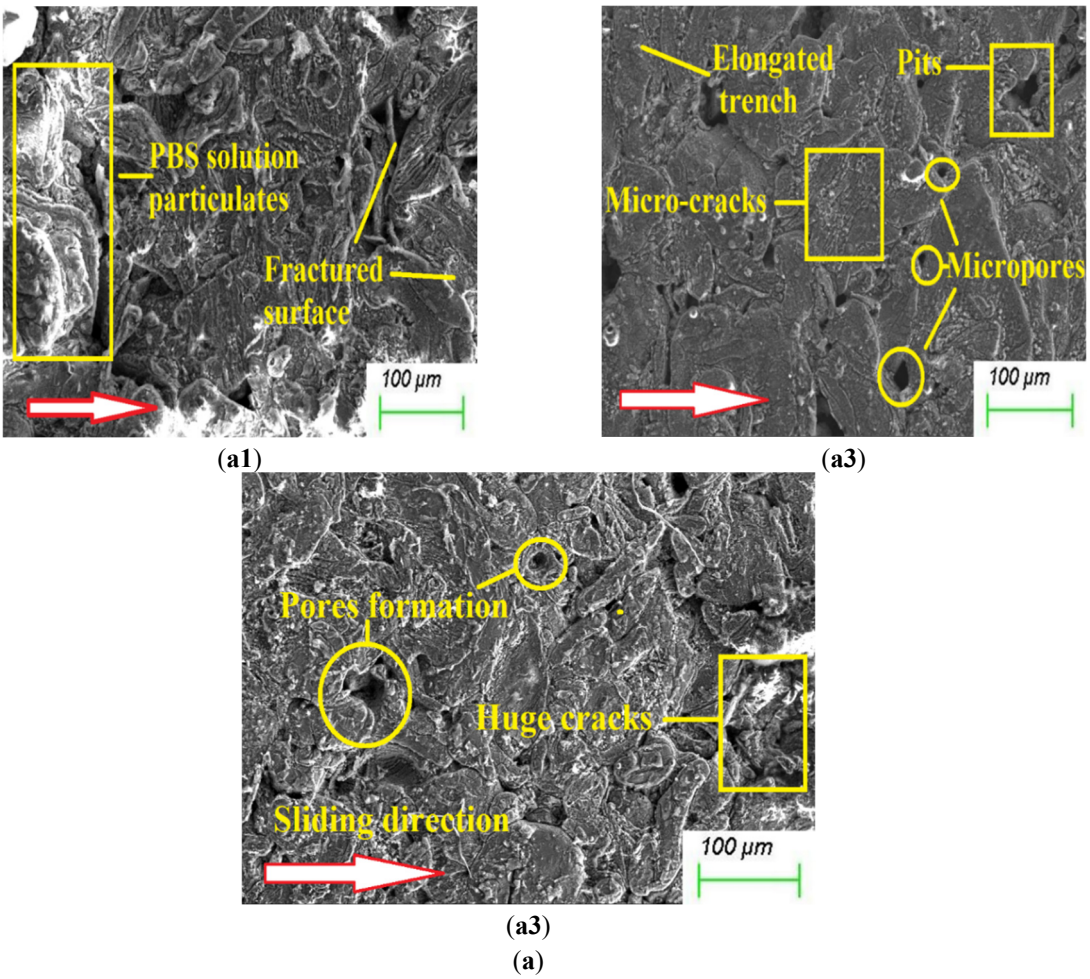

Figure 11. (**a**): Wear surface at sliding velocity 20 N load (**a1**) Mg-HAP-1Nd_2O_3 (**a2**) Mg-HAP-1.5Nd_2O_3 (**a3**) Mg-HAP-2Nd_2O_3 (**b**) Progressive wear rate plot for composite samples at 20 N load.

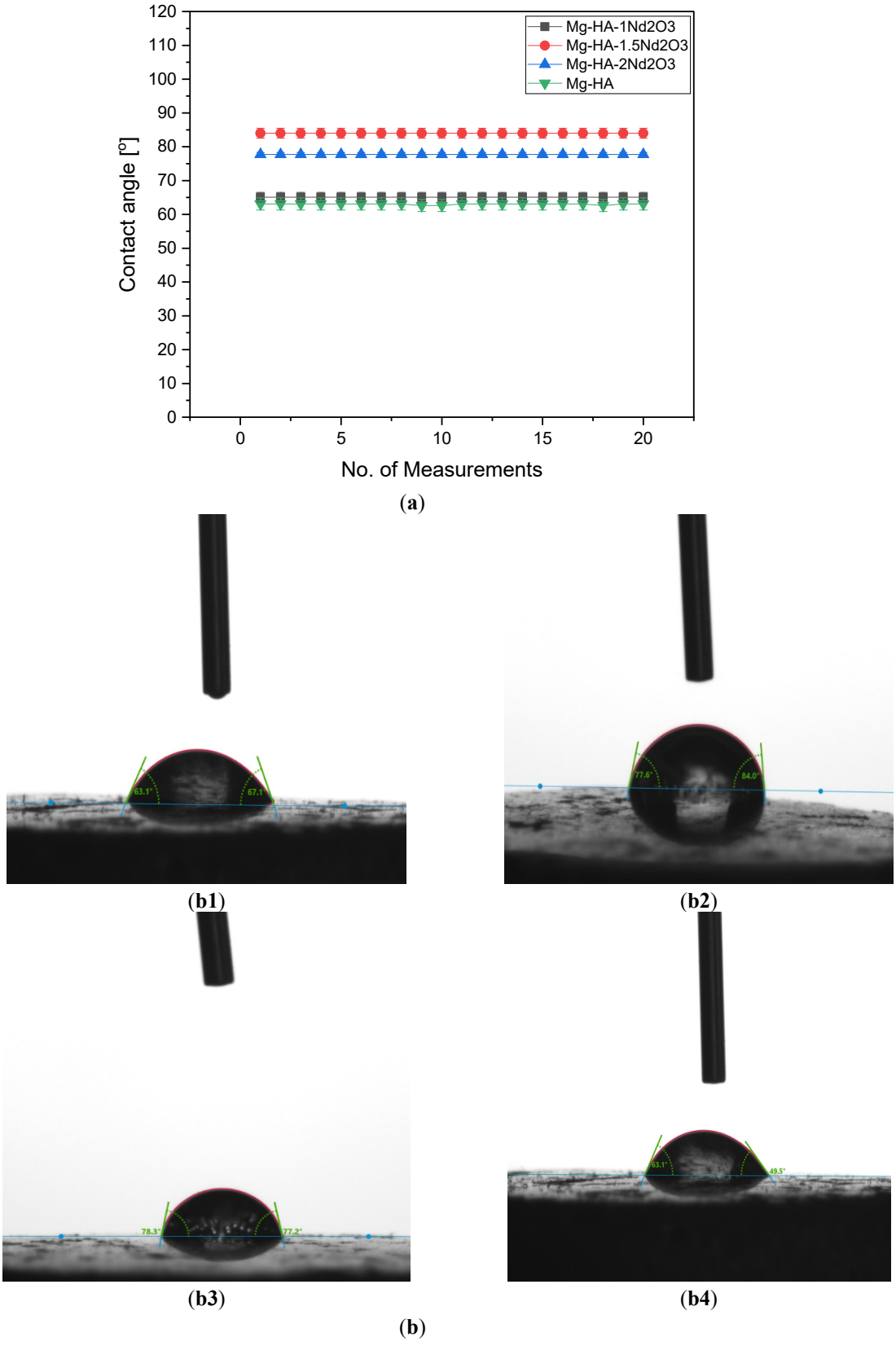

Figure 12. (**a**): Contact angle measurements of composite samples using sessile drop analyzer. (**b**) Schematic configuration of sessile drop contact angle measurements for (**b1**) Mg-HA-1Nd_2O_3 (**b2**) Mg-HA-1.5Nd_2O_3 (**b3**) Mg-HA-2Nd_2O_3 (**b4**) Mg-HA composite.

4. Conclusions

The current study showcased the design of a novel technique to determine the wear rate of Mg-HA-xNd_2O_3 (x: 1%, 1.5%, and 2%) fabricated through the powder metallurgy technique. The developed technique provided

analysis of the wear mechanism of the fabricated samples by sliding against a frictional disc under a physiological environment. Moreover, for subsequent analysis of wear rate, the specimens were subjected to different loads (10 N, 15 N, and 20 N) at different sliding velocities (1, 1.5, and 2 m/s). Henceforth, various conclusions can be drawn from the experimental studies.

(1) The maximum hardness was achieved for the sample incorporated with 1.5% Nd_2O_3 with an average hardness value of 42.413 HV, which was 2.35% and 9.72% more than Mg-HA-2Nd_2O_3 and Mg-HA-1Nd_2O_3, respectively. The primary cause for increased hardness was refined grain structure, and hard intermetallic compounds formed that provided resistance to indentation.

(2) Similarly, the tensile strength was highest with the sample consisting of 1.5% rare earth oxide with ultimate tensile strength (UTS) value of 154.23 MPa, followed by Mg-HA-2Nd_2O_3 and Mg-HA-1Nd_2O_3 with UTS values of 134.5 MPa and 141.01 MPa, respectively. Solid solution hardening, dislocation movement barricading, and solid solution hardening were fundamental reasons for increased strength.

(3) It was found that the samples having 1.5% rare earth oxide showed the highest wear resistance and lowest coefficient of friction compared to other samples. The wear rate followed the log phase in the initial stage, followed by a constant wear rate with an increase in sliding distance.

(4) A significant improvement in wear rate was found by incorporating 1.5% rare earth oxide by a factor of 85.17%, whereas, with 1% and 2% addition, the improvement was 35% and 29.14%, respectively, at 10 N load.

(5) At load 15 N, the composite sample containing 1.5% rare earth oxide showed 75% improvement in wear rate compared to composite samples containing 2% and 1% Nd_2O_3, which showed 31.25% and 28.15% improvement, respectively.

(6) As the load reached 15N, the wear rate enhanced, and the %age improvement was lowered, with Mg-HA-1.5Nd_2O_3 composite sample showing a 65.46% improvement in wear rate. Also, Mg-HA-1Nd_2O_3 and Mg-HA-2Nd_2O_3 depicted gain of 23% and 19.85%, respectively.

(7) It was observed that the significant reason for the increased wear resistance was the formation of secondary β-phases in the composite samples, which increased the surface integrity by reducing the surface cracks and other secondary defects. Moreover, the inclusion of PBS through the surface grooves and cracks shattered the composite sample from inside, producing maximum leaching of the particles. Hence, causing more wear to the samples.

(8) The surface hydrophobicity was seen to be improved by the addition of rare earth oxide to the Mg-HA sample with Mg-HA-1.5Nd_2O_3 showing lowest wettability with average contact angle value of 84°. In contrast, composite samples containing 1% and 2% Nd_2O_3 produced highly hydrophilic surfaces with contact angle values of 77.7° and 65.1°, respectively.

5. Future Work

The current work focuses on the wear behavior of the Mg-HA-xNd_2O_3 composites for Biomedical implant applications. However, for developing a balance between mechanical and biological properties, some biocompatibility analyses are required. Therefore, the current successful mechanical response of the developed composites will aid in moving towards the biocompatibility studies in future work.

Author Contributions

Conceptualization, D.A.; Methodology, D.A. and S.S.; software, D.A.; validation, D.A., S.S., and M.G.; formal analysis, D.A.; investigation, D.A.; resources, D.A. and S.S.; data curation, D.A.; writing—original draft preparation, D.A.; writing—review and editing, D.A.; visualization, D.A. and S.S.; supervision, S.S. and M.G.; project administration, S.S.; funding acquisition, not applicable. All authors have read and agreed to the published version of the manuscript.

Funding

No funding details available.

Institutional Review Board Statement

Not applicable

Informed Consent Statement

Not applicable

Data Availability Statement

The data presented in this study are available on request from the corresponding authors. The data are not publicly available due to privacy.

Acknowledgments

The authors would like to acknowledge Thapar institute of Engineering and technology, Patiala, India for the support provided for this research.

Conflicts of Interest

The authors declare no conflict of interest

References

1. Liu, Y.; Sinha, S.K. Wear performances and wear mechanism study of bulk UHMWPE composites with nacre and CNT fillers and PFPE overcoat. *Wear* **2013**, *300*, 44–54. https://doi.org/10.1016/j.wear.2013.01.102.
2. Moghadasi, M.S.; Mohd Isa, M.A.; Ariffin, M.Z.; et al. A review on biomedical implant materials and the effect of friction stir based techniques on their mechanical and tribological properties. *J. Mater. Res. Technol.* **2022**, *17*, 1054–1121. https://doi.org/10.1016/j.jmrt.2022.01.050.
3. Prasadh, S.; Suresh, S.; Ratheesh, V.; et al. *Biocompatibility of Metal Matrix Composites Used for Biomedical Applications*; Elsevier Ltd.: Amsterdam, The Netherlands, 2021; Volume 1, pp. 474–501. https://doi.org/10.1016/b978-0-12-803581-8.11834-x.
4. Kumar Balu, S.; Andra, S.; Jeevanandam, J.; et al. Emerging marine derived nanohydroxyapatite and their composites for implant and biomedical applications. *J. Mech. Behav. Biomed. Mater.* **2021**, *119*, 104523. https://doi.org/10.1016/j.jmbbm.2021.104523.
5. Monticelli, C.; Zucchi, F.; Tampieri, A. Triboelectrochemical behaviour of a Si_3N_4-TiN ceramic composite and a titanium alloy commonly used in biomedical applications. *Wear* **2009**, *266*, 327–336. https://doi.org/10.1016/j.wear.2008.07.005.
6. Witte, F.; Kaese, V.; Haferkamp, H.; et al. In vivo corrosion of four magnesium alloys and the associated bone response. *J. Biomater.* **2005**, *26*, 3557–3563. https://doi.org/10.1016/j.biomaterials.2004.09.049.
7. Shahabuddin, M.; Mofijur, M.; Rizwanul Fattah, I.M.; et al. Study on the Tribological Characteristics of Plant Oil-Based Bio-Lubricant with Automotive Liner-Piston Ring Materials. *Curr. Res. Green Sustain. Chem.* **2022**, *5*, 1–6. https://doi.org/10.1016/j.crgsc.2022.100262.
8. Chowdhury, M.A.; Hossain, N.; Masum, A.A.; et al. Surface Coatings Analysis and Their Effects on Reduction of Tribological Properties of Coated Aluminum under Motion with ML Approach. *Mater. Res. Express* **2021**, *8*, 086508. https://doi.org/10.1088/2053-1591/ac1c33.
9. Chowdhury, M.A.; Reza, M.S.; Hossain, N.; et al. Improvement of Corrosion Resistance of Galvanization/Nickel/Chrome Plating Low Carbon Steels in H_2SO_4 under Dynamic Condition. *Surf. Topogr. Metrol. Prop.* **2021**, *9*, 035018. https://doi.org/10.1088/2051-672X/ac19f0.
10. Chowdhury, M.A.; Shuvho, M.B.A.; Hossain, N.; et al. Friction and wear characteristics of ceramics composite under multidirectional motions. *Proc. Inst. Mech. Eng. Part J J. Eng. Tribol.* **2022**, *236*, 867–880. https://doi.org/10.1177%2F13506501211042146.
11. Gu, X.; Zheng, Y.; Cheng, Y.; et al. Biomaterials In vitro corrosion and biocompatibility of binary magnesium alloys. *Biomaterials* **2009**, *30*, 484–498. https://doi.org/10.1016/j.biomaterials.2008.10.021.
12. Aggarwal, D.; Kumar, V.; Sharma, S. Effect of rare earth oxide microparticles on mechanical, corrosion, antibacterial, and hemolytic behavior of Mg-Hydroxyapatite composite for orthopedic applications–A preliminary in-vitro study. *J. Biomed. Mater. Res. Part B Appl. Biomater.* **2023**, *111*, 1232–1246. https://doi.org/10.1002/jbm.b.35228.
13. Adekanmbi, I.; Mosher, C.Z.; Lu, H.H.; et al. Mechanical behaviour of biodegradable AZ31 magnesium alloy after long term in vitro degradation. *Mater. Sci. Eng. C* **2017**, *77*, 1135–1144. https://doi.org/10.1016/j.msec.2017.03.216.
14. Manakari, V.; Parande, G.; Doddamani, M.; et al. Evaluation of wear resistance of magnesium/glass microballoon syntactic foams for engineering/biomedical applications. *Ceram. Int.* **2019**, *45*, 9302–9305. https://doi.org/10.1016/j.ceramint.2019.01.207.
15. Mu, J.; Wang, H.; Qin, B.; et al. Improved wear and corrosion resistance of biological compatible TiZrNb films on biomedical Ti6Al4V substrates by optimizing sputtering power. *Surf. Coat. Technol.* **2021**, *428*, 127866. https://doi.org/10.1016/j.surfcoat.2021.127866.
16. Chirico, C.; Romero, A.V.; Gordo, E.; et al. Improvement of wear resistance of low-cost powder metallurgy β-titanium alloys for biomedical applications. *Surf. Coat. Technol.* **2022**, 128207. https://doi.org/10.1016/j.surfcoat.2022.128207.

17. Qiu, M.; Li, Y.; Chen, L.; et al. Effects of rare earth treatment on tribological properties of self-lubricating spherical plain bearings. *Wear* **2013**, *305*, 274–279. https://doi.org/10.1016/j.wear.2012.12.021.
18. Tatarko, P.; Kašiarová, M.; Chlup, Z.; et al. Influence of rare-earth oxide additives and SiC nanoparticles on the wear behaviour of Si3N4-based composites at temperatures up to 900 °C. *Wear* **2013**, *300*, 155–162. https://doi.org/10.1016/j.wear.2013.01.030.
19. Tatarko, P.; Kašiarová, M.; Dusza, J.; et al. Wear resistance of hot-pressed Si_3N_4/SiC micro/nanocomposites sintered with rare-earth oxide additives. *Wear* **2010**, *269*, 867–874. https://doi.org/10.1016/j.wear.2010.08.020.
20. Jäger, M.; Jennissen, H.P.; Dittrich, F.; et al. Antimicrobial and osseointegration properties of nanostructured titanium orthopaedic implans. *Materials* **2017**, *10*, 1–28. https://doi.org/10.3390/ma10111302.
21. Stemmer, P.; Fischer, A. Pathways of dissipation of frictional energy under boundary lubricated sliding wear of martensitic materials. *Lubricants* **2018**, *6*, 34. https://doi.org/10.3390/lubricants6020034.
22. Subramanian, S.M.; Vijayan, J.; Muthaiah, V. Tribological wear behaviour and hardness measurement of SiC, Al_2O_3reinforced Al. matrix hybrid composite. *J. Inst. Eng.* **2017**, *98*, 291–296. https://doi.org/10.1007/s40033-016-0134-8.
23. Lembang, M.S.; Yulizar, Y.; Sudirman, S.; et al. A Facile Method for Green Synthesis of Nd_2O_3 Nanoparticles Using Aqueous Extract of Terminalia Catappa Leaf. *AIP Conf. Proc.* **2018**, *2023*, 1–7. https://doi.org/10.1063/1.5064090.
24. Ahmadi, S.; Mohammadi, L.; Rahdar, A.; et al. Acid Dye Removal from Aqueous Solution by Using Neodymium(III) Oxide Nanoadsorbents. *Nanomaterials* **2020**, *10*, 556. https://doi.org/10.3390/nano10030556.
25. Chandrasekar, A.; Sagadevan, S.; Dakshnamoorthy, A. Synthesis and characterization of nano-hydroxyapatite (n-HAP) using the wet chemical technique. *Int. J. Phys. Sci.* **2013**, *8*, 1639–1645. https://doi.org/10.5897/IJPS2013.3990.
26. Gheisari, H.; Karamian, E.; Abdellahi, M. A novel hydroxyapatite -Hardystonite nanocomposite ceramic. *Ceram. Int.* **2015**, *41*, 5967–5975. https://doi.org/10.1016/j.ceramint.2015.01.033.
27. Pramanik, S.; Agarwal, A.K. Development of High Strength Hydroxyapatite for Hard Tissue Replacement. *Trends Biomater. Artif. Organs* **2005**, *19*, 46–51. https://doi.org/10.1016/j.ceramint.2005.10.025.
28. Ibrahim, A.; Magliulo, N.; Groben, J.; et al. Hardness, an Important Indicator of Bone Quality, and the Role of Collagen in Bone Hardness. *J. Funct. Biomater.* **2020**, *11*, 85. https://doi.org/10.3390/jfb11040085.
29. Alijani, S.; Anvari, A. Characterization of Implantation's Biomaterials Based on the Patient and Doctor Expectations. *Res. Med. Eng. Sci.* **2018**, *4*, 315–316. https://doi.org/10.31031/RMES.2018.04.000583.
30. Wang, X.; Chen, G.; Yang, W.; et al. Effect of Nd content on microstructure and mechanical properties of Grf/Al composite. *Mater. Sci. Eng. A* **2011**, *528*, 8212–8217. https://doi:10.1016/j.msea.2011.07.039.
31. Zohoor, M.; Givi, M.K.B.; Salami, P. Effect of processing parameter on fabrication of Al-Mg/Cu composites via friction stir processing. *Mater. Des.* **2012**, *39*, 358–365. https://doi.org/10.1016/j.matdes.2012.02.042.
32. Hossieni, S.A.; Ranjbar, K.; Dehmolaei, R.; et al. Fabrication of Al5083 surface composites reinforced by CNTs and cerium oxide nano particles via friction stir processing. *J. Alloy. Compd.* **2015**, *622*, 725–733. https://doi.org/10.1016/j.jallcom.2014.10.158.
33. Kujur, M.S.; Manakari, V.; Parande, G.; et al. Development of rare-earth oxide reinforced magnesium nanocomposites for orthopaedic applications: A mechanical/immersion/biocompatibility perspective. *J. Mech. Behav. Biomed. Mater.* **2021**, *114*, 104162. https://doi.org/10.1016/j.jmbbm.2020.104162.
34. Zhang, Z.; Chen, D.L. Consideration of Orowan strengthening effect in particulate-reinforced metal matrix nanocomposites: A model for predicting their yield strength. *Scr. Mater.* **2006**, *54*, 1321–1326. https://doi.org/10.1016/j.scriptamat.2005.12.017.
35. Gerhardt, L.; Boccaccini, A.R. Bioactive Glass and Glass-Ceramic Scaffolds for Bone Tissue Engineering. *Materials* **2010**, *3*, 3867–3910. https://doi.org/10.3390/ma3073867.
36. Henkel, J.; Woodruff, M.A.; Epari, D.R.; et al. Bone Regeneration Based on Tissue Engineering Conceptions—A 21st Century Perspective. *Bone Res.* **2013**, *1*, 216–248. https://doi.org/10.4248/BR20130300.
37. Sunil, B.R.; Reddy, G.P.K.; Patle, H.; et al. Magnesium based surface metal matrix composites by friction stir processing. *J. Magnes. Alloy* **2016**, *4*, 52–61. https://doi.org/10.1016/j.jma.2016.02.001.
38. Chen, J.; Tan, L.; Yu, X.; et al. Mechanical properties of magnesium alloys for medical application: A review. *J. Mech. Behav. Biomed. Mater.* **2018**, *87*, 68–79. https://doi.org/10.1016/j.jmbbm.2018.07.022.
39. Noviana, D.; Paramitha, D.; Fakhrul, M.; et al. ScienceDirect The effect of hydrogen gas evolution of Magnesium implant on the postimplantation mortality of rats. *J. Orthop. Transl.* **2016**, *5*, 9–15. https://doi.org/10.1016/j.jot.2015.08.003.
40. Zhao, D.; Wang, T.; Kuhlmann, J.; et al. In vivo monitoring the biodegradation of Magnesium alloys with an electrochemical H_2 sensor. *ACTA Biomater.* **2016**, *36*, 361–368. https://doi.org/10.1016/j.actbio.2016.03.039.
41. Sharma, V.K.; Kumar, V.; Joshi, R.S. Effect of RE addition on wear behavior of an Al-6061 based hybrid composite. *Wear* **2019**, *426–427*, 961–974. https://doi.org/10.1016/j.wear.2019.01.044.

42. Khan, S.; Candidate, S.M. Hydrophobicity of Rare-Earth Oxide Ceramics and Their Application in Promoting Sustained Dropwise Condensation and Corrosion and Fouling Mitigation in Hydropower Systems. 2015. Available online: https://www.osti.gov/servlets/purl/1638709 (accessed on 22 Dec 2022).
43. Sharma, V.K.; Kumar, V.; Joshi, R.S. Parametric study of aluminium-rare earth based composites with improved hydrophobicity using response surface method. *J. Mater. Res. Technol.* **2020**, *9*, 4919–4932. https://doi.org/10.1016/j.jmrt.2020.03.011.
44. Hass, K.C.; Schneider, W.F.; Curioni, A.; et al. The chemistry of water on alumina surfaces: Reaction dynamicsfrom first principles. *Science* **1998**, *282*, 265–268. https://doi.org/10.1126/science.282.5387.265.
45. Cohen, N.; Dotan, A.; Dodiuk, H.; et al. Superhydrophobic Coatings and Their Durability Superhydrophobic Coatings and Their Durability. *Mater. Manuf. Process.* **2016**, *31*, 1143–1155. https://doi.org/10.1080/10426914.2015.1090600.
46. Aggarwal, D.; Kumar, V.; Sharma, S. Effect of rare earth oxide microparticles on mechanical, corrosion, antibacterial, and hemolytic behavior of Mg-Hydroxyapatite composite for orthopedic applications—A preliminary in-vitro study. *J. Biomed. Mater. Res. Appl. Biomater*. **2023**, *111*, 1232–1246. https://doi.org/10.1002/jbm.b.35228.